

# Tensor network analysis of the maple-leaf antiferromagnet spangolite

Philipp Schmoll,<sup>1</sup> Harald O. Jeschke,<sup>2,3</sup> and Yasir Iqbal<sup>3</sup>

<sup>1</sup>*Dahlem Center for Complex Quantum Systems and Institut für Theoretische Physik, Freie Universität Berlin, Arnimallee 14, 14195 Berlin, Germany*

<sup>2</sup>*Research Institute for Interdisciplinary Science, Okayama University, Okayama 700-8530, Japan*

<sup>3</sup>*Department of Physics and Quantum Centre of Excellence for Diamond and Emergent Materials (QuCenDiEM), Indian Institute of Technology Madras, Chennai 600036, India*

Spangolite ( $\text{Cu}_6\text{Al}(\text{SO}_4)(\text{OH})_{12}\text{Cl}\cdot 3\text{H}_2\text{O}$ ) is a hydrated layered copper sulfate mineral whose crystal structure is well described by a depleted triangular lattice of  $\text{Cu}^{2+}$  ions in each layer. Experimental measurements reveal a non-magnetic ground state at  $T \sim 8$  K with magnetization properties dominated by dimerization. We propose a concrete model of  $\text{Cu}^{2+}$  spin-1/2 degrees of freedom on this geometrically frustrated and effectively two-dimensional maple-leaf lattice. The distorted geometry of the depleted triangular lattice layers results in a spatially anisotropic Heisenberg model featuring five symmetry inequivalent couplings with ferromagnetic bonds on hexagons and antiferromagnetic triangular bonds. The validity of the proposed Hamiltonian is demonstrated by state-of-the-art tensor network calculations which can assess both the nature of the ground state as well as low-temperature thermodynamics, including effects of a magnetic field. We provide theoretical support for a dimerized ground state by calculating the static spin structure factor as well as the magnetic susceptibility, the latter is shown to be in good agreement with experiment. We further predict the emergence of magnetisation plateaus at high values of an external magnetic field and study their melting with increasing temperature.

## INTRODUCTION

The kagome lattice antiferromagnet is the embodiment of high geometric frustration in two dimensions [1]. However, a number of other lattices based on triangular motifs come close if we consider suppression of ordered moment [2, 3]. Examples of other highly frustrated Archimedean lattices are the star, bounce, trellis and maple-leaf lattices. A common feature of these lattices is that material realizations are extremely rare [4]; metal-organic approximate versions exist for the star [5] and trellis lattice [6]. Concerning the maple-leaf lattice (MLL) (see Fig. 1a) [7], the situation is slightly more promising [8, 9] as a number of minerals with quantum spins like bluebellite  $\text{Cu}_6\text{IO}_3(\text{OH})_{10}\text{Cl}$  [10], mojaveite  $\text{Cu}_6\text{TeO}_4(\text{OH})\text{Cl}$  [10], fuetterite  $\text{Pb}_3\text{Cu}_6\text{TeO}_6(\text{OH})_7\text{Cl}_5$  [11], sabelliite  $(\text{Cu,Zn})_2\text{Zn}[(\text{As,Sb})\text{O}_4](\text{OH})_3$  [12] and spangolite  $\text{Cu}_6\text{Al}(\text{SO}_4)(\text{OH})_{12}\text{Cl}\cdot 3\text{H}_2\text{O}$  [13–16] have been found; besides, some semi-classical maple-leaf lattice antiferromagnets like  $\text{MgMn}_3\text{O}_7\cdot 3\text{H}_2\text{O}$  [17] and  $\text{Na}_2\text{Mn}_3\text{O}_7$  [18, 19] are known. Here, we focus on spangolite, which has been characterized magnetically [20] with evidence of a non-magnetic ground state. However, the nature of the singlet ground state remains a riddle with various speculative scenarios of either isolated or interacting dimers and trimers having been discussed in Ref. [2], but none found to be in complete agreement with observed magnetic features. In this manuscript, we address this long-standing issue by first employing ab-initio density functional theory (DFT) calculations to reliably ascertain the magnetic interactions, which are shown in Fig. 1a, and found to be antiferromagnetic on the dimer ( $J_1$ ) and triangular ( $J_4$  and  $J_5$ ) bonds, and ferromagnetic on the hexagons

( $J_2$  and  $J_3$ ). The resulting magnetic Hamiltonian is analyzed employing state-of-the-art tensor network (TN) simulations based on *infinite projected entangled simplex states* (iPESS) [21] and *infinite projected entangled simplex operators* (iPESOs) [22] ansätze, to assess both its ground state as well as finite magnetic field and finite-temperature behavior.

Our results lend support to a picture of a dimerized ground state characterized by strong singlet formation on the dimer bonds ( $J_1$  in Fig. 1a), which can be ascribed to the presence of large antiferromagnetic coupling on these bonds. Since these singlets are coupled via appreciable ferromagnetic correlations on the hexagons, they cannot be viewed as being isolated. The ground state is thus composed of correlated dimers and can be viewed as a dressed version of the exact dimer product state [23]. The behavior of the magnetic susceptibility with temperature is found to be in qualitative agreement with experiment, with the caveat that the non-magnetic ground state onsets at a comparatively higher temperature. The finding of a substantially reduced effective magnetic moment at high temperatures (in agreement with experiment) compared to that expected of six  $S = 1/2$  spins lends support to a ground state composed of non-trivially correlated dimers. This is indeed confirmed by the obtained ground state spin correlation profile, which features significant spin-spin correlations on the triangular and hexagonal bonds. We do not see any evidence of the formation of strongly bound clusters or trimers, which would require invoking additional orbital moments as speculated in Ref. [20]. Under the application of a magnetic field, the resulting magnetization curve displays plateaus at 1/3, 2/3, and 4/9 of the saturation magnetization characterized by a translationally invariant pattern of spin-spin correlations for the former two, and an eighteen site unit

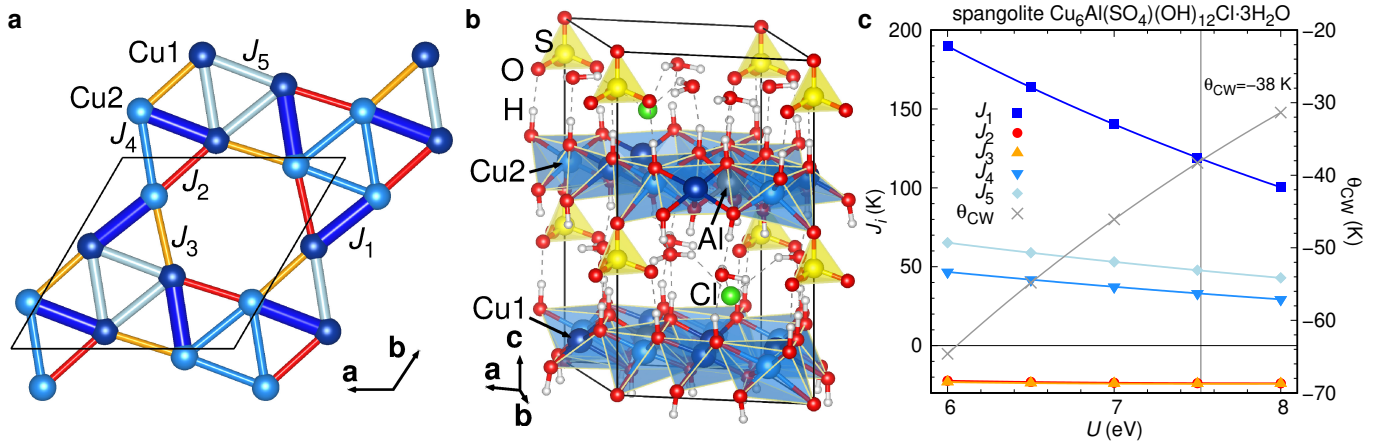


FIG. 1. **Structure and Heisenberg Hamiltonian parameters of spangolite.** **a** Distorted maple-leaf lattice realized in spangolite. The bonds represent the exchange interactions  $J_i$ , with thickness scaled in proportion to their values. **b** Crystal structure of spangolite  $\text{Cu}_6\text{Al}(\text{SO}_4)(\text{OH})_{12}\text{Cl}\cdot 3\text{H}_2\text{O}$  [20] with DFT relaxed hydrogen positions. **c** Five exchange interaction constituting the maple-leaf lattice, determined by DFT energy mapping, as function of on-site interaction strength  $U$ . The vertical line indicates the  $U$  value for which the couplings match the experimental Curie-Weiss temperature, and for this  $U$  we have antiferromagnetic  $J_1 = 118.4(2)$  K,  $J_4 = 33.0(2)$  K and  $J_5 = 47.6(2)$  K and ferromagnetic  $J_2 = -23.8(1)$  K and  $J_3 = -24.2(1)$  K.

cell for the  $4/9$  plateau. The temperature evolution of the magnetization curve shows a relatively faster melting of the  $1/3$  compared to the  $2/3$  plateau.

## RESULTS

### Heisenberg Hamiltonian

We begin our study of spangolite by determining the parameters of the Heisenberg Hamiltonian

$$H = \sum_{i < j} J_{ij} \mathbf{S}_i \cdot \mathbf{S}_j \quad (1)$$

using the density functional theory based energy mapping technique. This approach has proven instrumental for the understanding of various  $\text{Cu}^{2+}$  based minerals like centennialite [26], henmilitite [27], birchite [28], kapellasite [29] as well as  $\text{PbCuTe}_2\text{O}_6$  (idealized colocalite [30]) [31]. The first step is to establish the best possible crystal structure, including all hydrogen positions. For this purpose, we use the structure determined by Fennell *et al.* [20], adding to it the missing H3 position from Hawthorne *et al.* [16]. We then

name	$J_1$	$J_2$	$J_3$	$J_4$	$J_5$
value (K)	118.4(2)	-23.8(1)	-24.2(1)	33.0(2)	47.6(2)
$d_{\text{Cu-Cu}}$ (Å)	3.005	3.107	3.110	3.213	3.216

TABLE I. **Exchange interactions of spangolite  $\text{Cu}_6\text{Al}(\text{SO}_4)(\text{OH})_{12}\text{Cl}\cdot 3\text{H}_2\text{O}$  obtained by DFT energy mapping.** The couplings are interpolated to  $U = 7.52$  eV so that they match the experimental Curie-Weiss temperature  $\theta_{\text{CW}} = -38$  K [20]. The Cu-Cu distances are given to identify the exchange path.

carefully relax all six hydrogen positions using the full potential local orbital (FPLO) code [32] and the generalized gradient approximation (GGA) [33] exchange correlation functional. The resulting crystal structure is shown in Fig. 1 b. The structure is characterized by  $\text{Cu}^{2+}$  maple-leaf layers where  $\text{Al}^{3+}$  ions fill the centers of the hexagons. The metal hydroxide layers are well separated by sulfate groups and water molecules, indicating a high level of two-dimensionality of the material.

We now proceed to extract the Heisenberg Hamiltonian parameters of Eq. (1) by calculating 40 out of 364 distinct energies for the possible spin configurations in the unit cell, where we lower the symmetry to  $P1$  in order to make all twelve  $\text{Cu}^{2+}$  sites symmetry inequivalent. This allows us to resolve the five nearest-neighbour exchange interactions which make up the distorted maple-leaf lattice of spangolite. We also resolve seven longer range couplings which turn out to be less than one percent of the largest coupling and which we ignore in our subsequent analysis. The values of the first five exchange interactions are plotted in Fig. 1 c as function of the on-site interaction strength  $U$ . The relevant value of  $U$ , determined by demanding that the mean-field estimate of the Curie-Weiss temperature matches the experimental value of  $\theta_{\text{CW}} = -38$  K [20] is marked by a vertical line. The resulting Hamiltonian parameters, which are the basis for our further investigation are given in Table I. Spangolite is found to be characterized by a unique network of three antiferromagnetic and two ferromagnetic couplings shown in Fig. 1 a. The largest coupling, antiferromagnetic  $J_1$ , defines dimers. The two weaker antiferromagnetic couplings  $J_4 = 0.278J_1$  and  $J_5 = 0.402J_1$  define triangles, and the two ferromagnetic couplings  $J_2 = -0.201J_1$  and  $J_3 = -0.204J_1$  form the

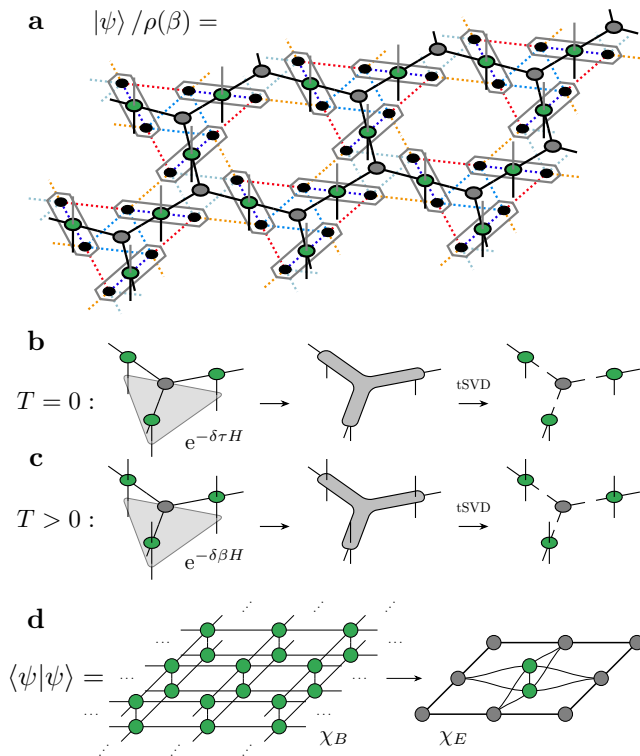


FIG. 2. **Tensor network setup for the simulations of spangolite.** **a** Infinite projected entangled simplex state and operator ansatz for the simulations of spangolite. A coarse-graining of the two spins on  $J_1$  bonds results in a regular kagome lattice, on which the tensor network is defined. While quantum states  $|\psi\rangle$  have one physical index (represented by the black vertical lines), thermal states  $\rho(\beta)$  need two physical indices (both black and gray virtual lines). **b** & **c** Simple update step for the iPESS ground state ( $T = 0$ ) and iPESO thermal state ( $T > 0$ ). The imaginary time evolution gate is first absorbed into a triangle configuration to evolve the states. Applying a higher-order singular value decomposition (SVD) with truncation (tSVD) to the bulk bond dimension  $\chi_B$  recovers the individual tensors. **d** Coarse-graining the six spins in the elementary unit cell results in a square lattice TN, whose contraction is approximated by fixed-point environment tensors shown in gray, using a corner transfer matrix renormalization group procedure. The unavoidable approximations are controlled by an environment bond dimension  $\chi_E$ .

hexagons of the maple-leaf lattice. In the following, we will analyze the properties of this Hamiltonian using state-of-the-art tensor network techniques.

### Tensor network ansatz

The study of the spangolite Hamiltonian is based on numerical tensor network simulations in the thermodynamic limit. TNs are efficient representations of quantum many-body systems, that encode the probability amplitudes of a (thermal) quantum state as a contraction of a network of local tensors. The tensors are interconnected by auxiliary, virtual indices as shown in Fig. 2 a, whose

maximal dimension is called the *bond dimension*  $\chi_B$  of the TN (bulk bond dimension). It is a control parameter that can be systematically increased to improve the accuracy of the ansatz. Tuning the bond dimension changes the number of variational parameters in the TN and thereby the amount of quantum entanglement that can be captured. Tensor networks offer efficient numerical simulations with only a polynomial scaling in the number of particles, thus overcoming the exponential barrier by targeting the low-entanglement sector of the full Hilbert space [34, 35]. In our study, we employ *infinite projected entangled simplex states* (iPESS) [21] and *infinite projected entangled simplex operators* (iPEPO) [22] for the simulation of ground states and thermal states, respectively. In this context, the TN is used as an ansatz for the full many-body system, consisting of a unit cell of different tensors that generates a translationally invariant quantum state.

Upon coarse-graining the two spins on the dominant antiferromagnetic  $J_1$  bonds in the maple-leaf lattice, the system is mapped to a regular kagome lattice. Due to its corner-sharing triangles, a TN setup on the dual honeycomb lattice in the form of iPESS and iPEPO is very well suited to capture the multipartite quantum correlations therein. The general TN setup is shown in Fig. 2 a, where the stretched hexagons denote coarse-grained lattice sites, each represented by a single green tensor in b and c. In the chosen TN ansatz, those tensors reside on the links of the honeycomb lattice, so that additional three-index simplex tensors have to be introduced to connect them (gray tensors). Quantum states, represented by an iPESS, have only a single physical index per lattice site tensor, while thermal density matrices, represented by an iPEPO, have two. This is shown in the figure as black, and both black and gray indices, respectively. A single unit cell consists of three lattice tensors (capturing six spins), together with two simplex tensors. Importantly, tensor networks in the thermodynamic limit offer the possibility of choosing arbitrary unit cells, that are repeated periodically to generate the 2D lattice. This gives us the possibility to determine the actual structure of the targeted states based on energy comparisons of different configurations [36]. Each elementary unit cell of the honeycomb TN can be further coarse-grained into an effective tensor on a regular square lattice. This is important to compute accurate expectation values, for which we use a *corner transfer matrix renormalization group* (CTMRG) [37–39] procedure, as shown in Fig. 2 d. The contraction of the infinite square lattice introduces an additional control parameter, the environment bond dimension  $\chi_E$ . In our simulations we use system sizes of six, twelve and eighteen spins. Both ground and thermal state simulations are based on the very efficient simple update procedure [21, 22, 40, 41]. It is an approximate, yet reliable algorithm frequently used in TN simulations. Details about the simple update for iPESS and iPEPO, as well as the calculation of expectation values are

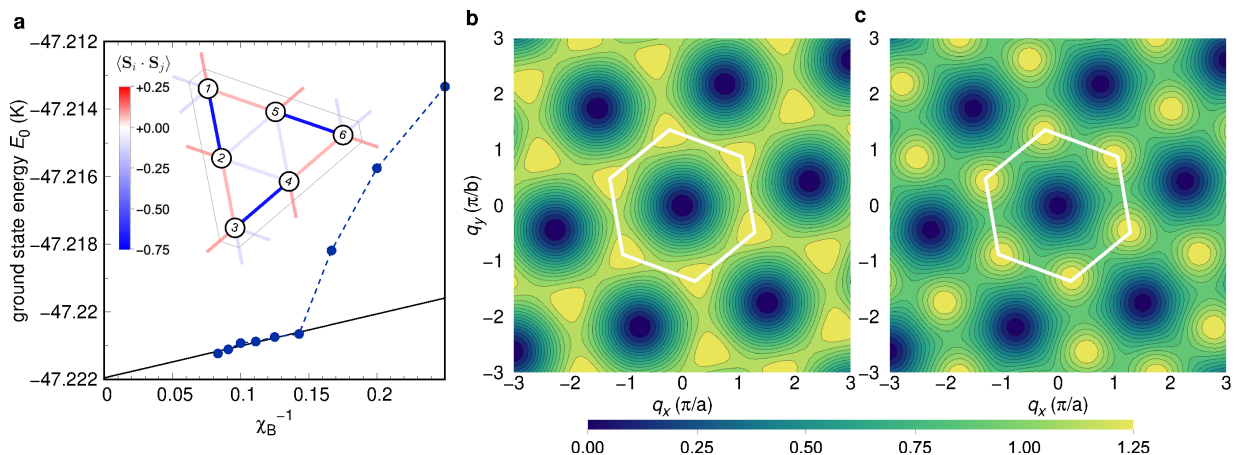


FIG. 3. **Ground state of spangolite.** **a** Ground state energy vs. inverse bond dimension  $\chi_B$  for the ground state of the spangolite Hamiltonian without magnetic field. The inset shows the spatial pattern of nearest-neighbour spin-spin correlations, revealing the strong dimerization. **b** The equal-time spin structure factor  $S(\mathbf{q})$  for an exact dimer state on  $J_1$  bonds [24, 25] and **c** for the ground state of the spangolite Hamiltonian at bond dimension  $\chi_B = 6$ . The extended Brillouin zone is marked by a white hexagon.

presented in the appendix.

### Ground state without magnetic field

The ground state for the spangolite Hamiltonian can be represented with a single geometrical unit cell of six spins. Due to the strong antiferromagnetic interaction on  $J_1$  bonds, it is dominated by a dimerization of the connected spins. The remaining antiferromagnetic interaction terms contribute only weakly to the structure, however, there exist nonnegligible ferromagnetic correlations on the hexagonal bonds. Due to the chosen coarse-graining, the two spins on  $J_1$  bonds are treated exactly as a single tensor site, and entanglement with neighbouring sites is only weak. The chosen TN ansatz is therefore ideal and the simple update algorithm leads to accurate results. More sophisticated procedures, such as variational optimisation [42] are limited to smaller bond dimensions and not superior here. The ground state energy vs. the inverse iPES bond dimension is shown in Fig. 3 a. Quantum correlations are already seen to be well captured with an ansatz of  $\chi_B = 8$ , and a larger bond dimension does not substantially decrease the energy further. A fit of the six largest data points reveals a good estimate for the infinite bond dimension limit ( $\chi_B \rightarrow \infty$ ), for which we extrapolate to an energy of

$$E_0/J_1 = -0.39883(4). \quad (2)$$

The energy is found to be lower compared to that of an exact dimer product state (on  $J_1$  bonds), which has an energy per site of  $E/J_1 = -0.375$ . The spatial pattern of nearest-neighbour spin-spin correlations  $\langle \mathbf{S}_i \cdot \mathbf{S}_j \rangle$  reveals the expected strong dimerization of the ground state on  $J_1$  bonds. It is shown as the inset of Fig. 3 a. The spins on the hexagons show weak ferromagnetic alignment, while the spins on triangle configurations are nearly uncorrelated. Thus, the ground state cannot be characterized by

isolated singlet formations on the dimer bonds alone, but instead these dimers are correlated (due to ferromagnetically correlated hexagonal bonds) forming a correlated dimer liquid with a lower energy.

In order to further characterize the ground state, we compute the equal-time spin structure factor

$$S(\mathbf{q}) = \sum_{i,j} \sum_{m,n} e^{i\mathbf{q} \cdot (\mathbf{R}_i - \mathbf{R}_j)} e^{i\mathbf{q} \cdot (\mathbf{b}_m - \mathbf{b}_n)} \times \langle \mathbf{S}(\mathbf{R}_i + \mathbf{b}_m) \cdot \mathbf{S}(\mathbf{R}_j + \mathbf{b}_n) \rangle. \quad (3)$$

Here,  $(i, j)$  denotes the summation over unit cells and  $(m, n)$  the additional summation over the six-site basis of the maple-leaf lattice. By exploiting translational invariance, one sum over unit cells can be removed, and the structure factor can be computed by a CTMRG resummation scheme [43–45], accounting for the appropriate phase factors and spin operators while absorbing tensors into the environment tensors. This scheme typically needs large environment bond dimensions  $\chi_E$  to reach convergence. However, due to the large gap in our system (cf. the width of the zero-magnetisation plateau below), the calculations of the structure factor can be converged with moderate  $\chi_E$ . In order to have a defined reference, we show the structure factor for the spangolite ground state in comparison to an exact dimer state on  $J_1$  bonds in Fig. 3 b and c. While the exact dimer state is representable with an iPES at bond dimension  $\chi_B = 1$ , i.e., a product state of coarse-grained dimers, the structure factor for spangolite is computed at  $\chi_B = 6$  to balance accuracy and the computational cost of the CTMRG routine. The similarity in the structure factor for the spangolite ground state with the exact dimer one confirms the strong dimerization, however, it is slightly smeared compared to the exact dimer state.

### Thermal state and heat capacity

Before investigating magnetic properties of the spangolite Hamiltonian, we compute thermal state properties without a magnetic field using iPESO simulations at a large bulk bond dimension  $\chi_B = 32$  with mean-field environments [22]. Thermal states are obtained by successively cooling an infinite-temperature state with infinitesimal steps  $\delta\beta = 10^{-3}$  down to low temperatures. From the thermal state energy we can compute the heat capacity  $C = \partial U / \partial T$ . Results are shown in Fig. 4 a.  $C/T$  features a pronounced peak at  $T \sim 30$  K.

In the inset we show the thermal state energy alongside the truncation error in the simple update cooling procedure. The thermal state energy converges to the ground state energy of Fig. 3 a for low temperatures, indicating that the procedure does not get stuck in local minima during the cooling. The truncation error can be used to probe the accuracy of the simulations. It stays below  $\varepsilon \sim 10^{-2}$  down to  $T = 1$  K, which is a good indication that the chosen bond dimension for the thermal state simulations is sufficiently high.

### Magnetic susceptibility

To further characterize the spangolite Hamiltonian, we computed the variation of the magnetic susceptibility with temperature using the iPESO thermal state algorithm. To this end, we choose a very accurate infinitesimal temperature step of  $\delta\beta = 10^{-4}$  and a large bulk bond dimension of  $\chi_B = 24$ . Expectation values are again computed using the mean-field environment, which is reasonable due to the high bond dimension and temperature, and low entanglement in the system. Fortunately, we can directly compare our theoretical simulations of the model Hamiltonian to experimental measurements on spangolite. The magnetic susceptibility is computed from the magnetization along the direction of the field according to

$$\chi_M(T) = \left. \frac{\partial m_z(T)}{\partial h_z} \right|_{h_z \rightarrow 0}. \quad (4)$$

Our results, alongside the data extracted from Ref. [20] are shown in Fig. 4 b. The main feature of a sharp peak and a high-temperature tail is correctly recovered by our tensor network simulations. A numerical fit of the high-temperature regime ( $T > 400$  K for the simulation,  $T > 100$  K for the experiment) with a Curie-Weiss law

$$\chi_M(T) = \frac{C}{T - \theta_{CW}} \quad (5)$$

is used to extract the Curie-Weiss temperature  $\theta_{CW}$ . The fit results in parameters given in Table II. The simulations show a quicker decline of the magnetic susceptibility, indicating a non-magnetic ground state already at higher temperatures. From the Curie-Weiss constant  $C$  we can compute the effective magnetic moment

$$\mu_{\text{eff}} = \sqrt{\frac{3k_B C}{N_A \mu_B^2}}. \quad (6)$$

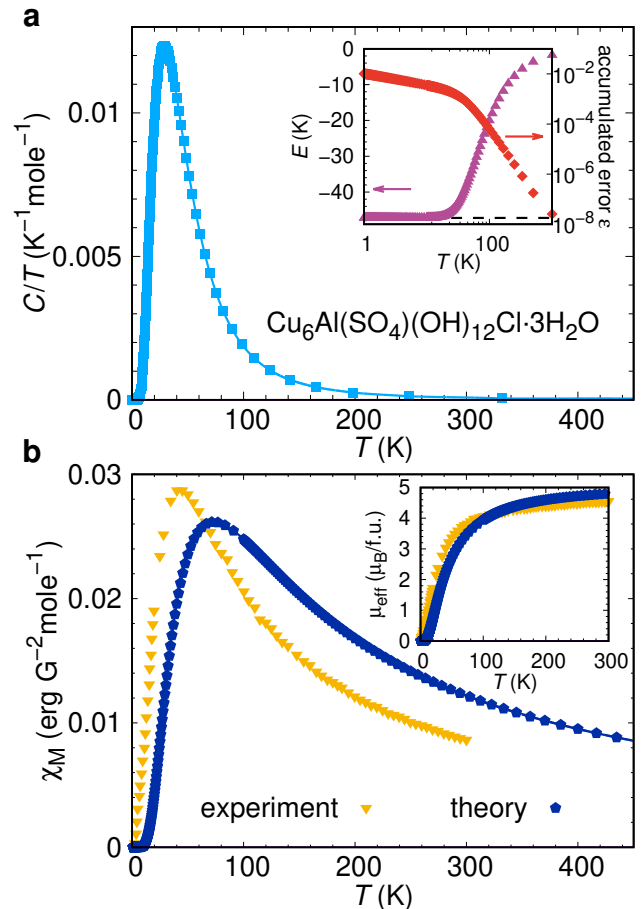


FIG. 4. **Thermodynamic properties of spangolite.** **a** Specific heat divided by temperature showing a pronounced peak at  $T \sim 30$  K. The inset shows the thermal state energy, that converges to the ground state energy for low temperatures, alongside the accumulated truncation error of the simple update cooling procedure, that stays below  $\varepsilon \sim 10^{-2}$  throughout the full range of temperatures. **b** Magnetic susceptibility over temperature. The high-temperature regime ( $T > 400$  K for the simulation,  $T > 100$  K for the experiment) is fitted with a Curie-Weiss law to extract the CW temperature in Table II. The inset shows the effective magnetic moment. Details are given in the text.

	experiment	simulation
$C$	2.98 K	4.25 K
$\theta_{CW}$	-45.2 K	-46.5 K
$\mu_{\text{eff}}$	4.79(1) $\mu_B$ /f.u.	5.83 $\mu_B$ /f.u.

TABLE II. Parameters of the numerical fit of the Curie-Weiss law of the magnetic susceptibility. Experimental data has been extracted from Ref. [20]. The effective magnetic moment  $\mu_{\text{eff}}$  is computed according to Eq. (6) in the units of  $\mu_B$  per formula unit.

The extracted value from the TN simulations is slightly larger compared to the experimentally estimated one, see Table II. In particular, the substantial reduction in  $\mu_{\text{eff}}$  compared to the expected value for the spangolite formula unit, which has  $\mu_{\text{eff}} = 10.39 \mu_B$ /f.u. for the six

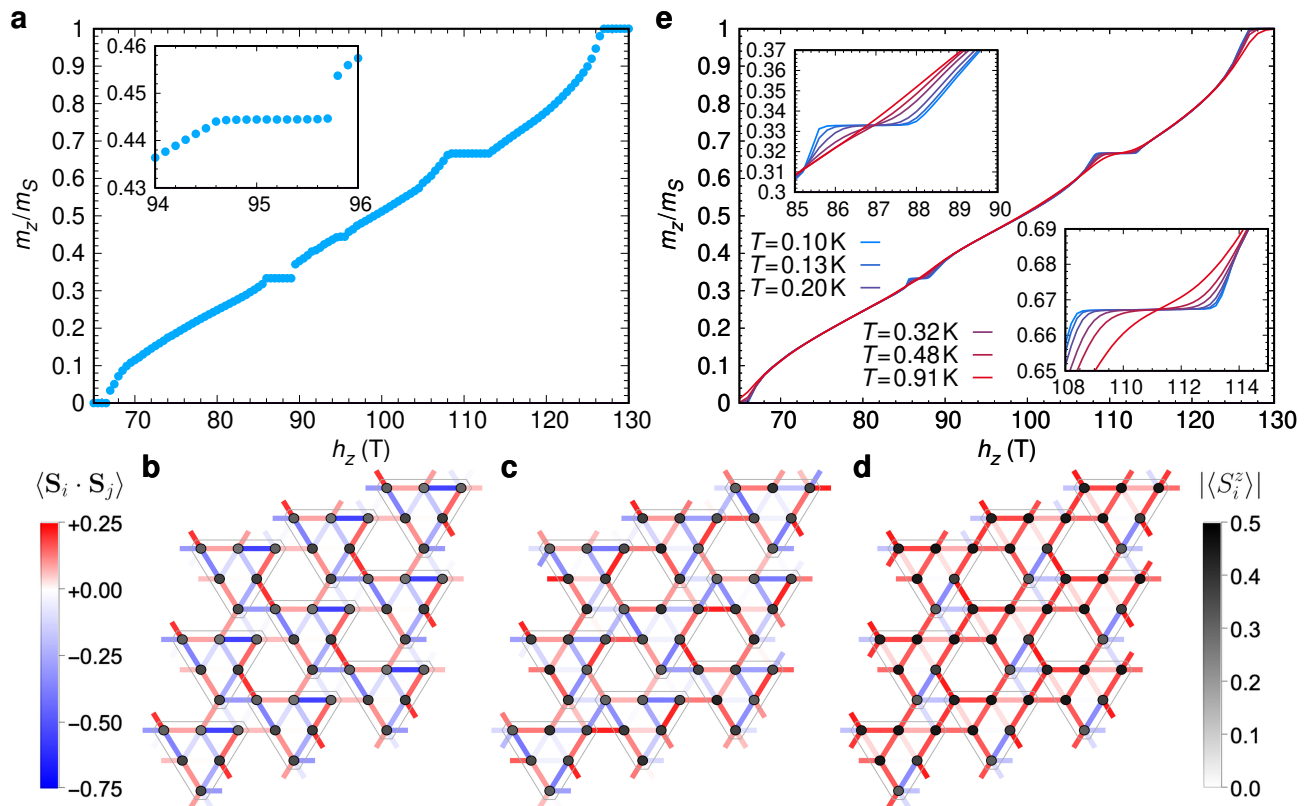


FIG. 5. **Magnetization curves of spangolite.** Zero temperature magnetization of the spangolite Hamiltonian over the magnetic field  $h_z$  at  $\chi_B = 8$ , using CTMRG environments. Below  $h_z \sim 67$  T the strong antiferromagnetic  $J_1$  interaction leads to a vanishing magnetization. Three plateaus at  $1/3$ ,  $4/9$  and  $2/3$  of the saturation  $m_S = 1/2$  are found. The inset shows the narrow  $4/9$  plateau. **b-d** Nearest-neighbour spin-spin correlations and local  $S^z$  expectation values for the  $1/3$ ,  $4/9$  and  $2/3$  magnetization plateaus, corresponding to values of **b**  $h_z = 90$ , **c**  $h_z = 95$  and **d**  $h_z = 110$ , respectively. **e** Magnetisation curve of spangolite at finite temperatures. The insets show the melting of the  $m_z/m_S = 1/3$  and  $2/3$  magnetisation plateaus as an effect of increasing temperature.

spin- $1/2s$  [20], is reflective of the fact that the ground state cannot be viewed as either being composed of isolated dimers or explained by a model of dimers interacting with a mean-field [46–48] – in consonance with the description of the ground state obtained from TN simulations. This, alongside the vanishing susceptibility at a higher temperature indicates an overestimation of the formation of dimers, which could result from a slightly too high value for  $J_1$  in the model Hamiltonian. The iPESO ansatz itself is biased towards the formation of dimers on  $J_1$  bonds as well, however, the large bulk bond dimension  $\chi_B = 24$  should allow sufficient correlations to neighbouring sites to counteract this bias. Using  $C = \chi_M T$  in Eq. (6), we can plot the effective magnetic moment over temperature as shown in the inset of Fig. 4 b. While both experiment and simulation data is not converged for high temperatures, our result settles in higher and in a similar range as experimental value, in agreement with the preceding discussion.

### Magnetization plateaus

Finally, we study the spangolite Hamiltonian in an external magnetic field. Due to the strong antiferromag-

netic interaction on  $J_1$  bonds, the system retains a non-magnetic ground state up until  $h_z \sim 65$  T. In the  $T = 0$  K simulations we have used unit cells of six, twelve and eighteen spins in order to capture more complicated ground state structures. The magnetization curve is then obtained from the states which minimize the energy. Upon tuning the magnetic field, we find the emergence of magnetisation plateaus at values of  $m_z/m_S = 1/3$ ,  $4/9$  and  $2/3$  of the saturation value  $m_S = 1/2$ . The full magnetisation curve is shown in Fig. 5 a. It is interesting to note that we do not find the  $1/6$ ,  $2/9$  and  $2/7$  plateaus observed in the magnetization curve of the exact dimer product ground state [49]. This provides further evidence that the ground state of the spangolite Hamiltonian is not formed by isolated singlets but more appropriately viewed as a correlated dimer state due to the presence of ferromagnetic correlations on the hexagonal bonds connecting the dimers.

While the spin-spin correlations in the  $1/3$  and  $2/3$  plateaus are translationally invariant and thus representable within a six site unit cell, the  $4/9$  plateau state is only captured by a unit cell of eighteen spins. All these three plateaus satisfy the conventional con-

dition for a magnetization plateau to emerge, namely,  $N_u S(1 - m_z/m_s) \in \mathbb{Z}$  [50, 51], where  $N_u$  is the number of sites in the unit cell for the ground state and  $S$  is the spin quantum number which, in the present case, is  $S = 1/2$ . For the aforementioned quantities, we obtain values of 2, 1, and 5 for the 1/3, 2/3, and 4/9 plateaus, respectively. The spatial pattern of spin-spin correlations and  $z$ -component of the magnetisation is shown in Fig. 5 b-d. Finally, we analyse the stability of the two prominent plateaus at  $m_z/m_s = 1/3$  and  $2/3$  with respect to temperature. To this end, we simulate the spangolite Hamiltonian in a field over a temperature range  $T \in [0.1 \text{ K}, 1000 \text{ K}]$  at a fixed bond dimension of  $\chi_B = 24$  using mean-field environments to compute expectation values. The unit cell is set to six spins, so that the additional, small 4/9 plateau cannot be captured. While the infinite-temperature states are fully disordered without any magnetization, the simple update cooling procedure recovers the two focused plateaus at low temperatures. A set of fixed temperature slices is shown in Fig. 5 e. In the inset we show the melting of both plateaus. Noticeably, they melt rather symmetrically from the low and high field limits, respectively. Due to the smaller width, the 1/3 magnetisation plateau is more susceptible to thermal effects and starts melting sooner than the 2/3 plateau.

## DISCUSSION

Employing a combination of density functional theory based energy mapping and tensor network simulations, we investigated the ground and thermal state properties in the presence of a magnetic field of a distorted maple-leaf lattice as realized in spangolite ( $\text{Cu}_6\text{Al}(\text{SO}_4)(\text{OH})_{12}\text{Cl}\cdot 3\text{H}_2\text{O}$ ). The DFT Hamiltonian features the largest coupling, antiferromagnetic  $J_1$  on the dimer bonds, while the subleading antiferromagnetic couplings,  $J_4 = 0.278J_1$  and  $J_5 = 0.402J_1$  define the triangles. An noteworthy aspect of the Hamiltonian is the presence of substantial ferromagnetic interactions,  $J_2 = -0.201J_1$  and  $J_3 = -0.204J_1$  on the hexagons. The pattern of spin-spin correlations in the ground state consequently features strong singlet formation on the dimer bonds, and sizeable ferromagnetic correlations on the hexagonal bonds which connect the dimers. Interestingly, the spins on the triangles are nearly uncorrelated. Thus, our picture of a non-trivially correlated dimer ground state accounts for the appreciable reduction in magnetic moment at high temperatures observed in experiment, thereby resolving a long-standing puzzle. It also effectively rules out a scenario of a ground state composed of either isolated dimers or dimers interacting with a mean-field, and dispenses with the need of invoking more complicated mechanisms which have been speculated about earlier. We find an excellent agreement with the experimentally observed behavior of the magnetic susceptibility. The magnetization curve of spangolite does not show the presence of 1/6, 2/9, and 2/7 plateaus which are ex-

pected for an exact dimer product configuration. This lends further evidence of a correlated dimer ground state. We find that the 1/3 and 2/3 plateau states are translation invariant, while the 4/9 state is described by an eighteen site unit cell. With increasing temperature, the 2/3 plateau appears more robust compared to the 1/3 plateau.

Much of the recent theoretical efforts in search of exotic non-magnetic states on the maple-leaf lattice have focused on the purely antiferromagnetic model [25, 52, 53]. However, lately the explorations of models with mixed ferro-antiferro couplings (with antiferromagnetically coupled hexagons and ferromagnetic coupling on triangles and dimer bonds) have unveiled a variety of dimer orders encompassing an island of putative quantum spin liquid behavior [54]. In similar vein, there could be a putative quantum spin liquid lurking around the corner proximate to the observed correlated dimer ground state. To this end, it would be worthwhile to perform a thorough investigation of the mixed ferro-antiferro parameter space of the spangolite Hamiltonian, which instead features ferromagnetically coupled hexagons and antiferromagnetic coupling on triangles and dimer bonds. This might also enable us to ascertain whether the observed dimerized phase could potentially be viewed as an instability of proximate quantum spin liquids, which have lately been classified in Ref. [55].

Our study of spangolite is the second detailed elucidation of the Hamiltonian of a maple-leaf material, the first being the recent investigation of bluebellite [24]. Both minerals share the distortion pattern of the ideal maple-leaf lattice with five inequivalent nearest-neighbor bonds and the fact that the Hamiltonian is dominantly antiferromagnetic, but modified by two ferromagnetic exchange interactions. As the resultant physics, spin singlet formation versus valence bond solid ground state for spangolite and bluebellite, respectively, vary considerably, it is a worthwhile endeavor to understand the other known copper minerals with maple-leaf lattice, mojaveite, fuetterite and sabelliite, as well. Their maple-leaf lattices are also distorted, promising new patterns of antiferromagnetic and ferromagnetic bonds. The example of bluebellite [17] suggests that synthesis of the minerals is possible and can lead to a reduction of the lattice distortions. A next step could be efforts to synthesize material variations, for example by replacing chlorine by bromine and thus to further extend the richness of quantum spin systems with maple-leaf structure.

From a methodological perspective, the tensor network methods employed make inroads into the extremely challenging problem of simulating the low-temperature thermodynamics of quantum spin models, in particular, modelling real quantum materials. These cross-benchmarking efforts advance both theory or simulation and condensed matter experiments, and help to build confidence in the results. The versatility of the employed framework can be further extended to include e.g., next-to-nearest neighbour interactions or applied to the study of layered quan-

tum materials [22, 56, 57], and are therefore readily available for the study of more elaborate model Hamiltonians.

### ACKNOWLEDGMENTS

We acknowledge helpful discussions with Jan Naumann and Tobias Müller. This work has been funded by the Deutsche Forschungsgemeinschaft (DFG, German Research Foundation) under the project number 277101999 – CRC 183 (project B01) and the BMBF (MUNIQC-Atoms, FermiQP). The authors would like to thank the HPC Service of ZEDAT, Freie Universität Berlin for computing time [58]. The research of Y.I. was carried out, in part, at the Kavli Institute for Theoretical Physics in Santa Barbara during the “A New Spin on Quantum Magnets” program in summer 2023, supported by the National Science Foundation under

Grant No. NSF PHY 1748958. The work of Y.I. was also performed, in part, at the Aspen Center for Physics, which is supported by National Science Foundation Grant No. PHY-2210452. The participation of Y.I. at the Aspen Center for Physics was supported by the Simons Foundation. Y.I. also acknowledges support from the ICTP through the Associates Programme and from the Simons Foundation through Grant No. 284558FY19, IIT Madras through the Institute of Eminence (IoE) program for establishing QuCenDiEM (Project No. SP22231244CPETWOQCDHOC), and the International Centre for Theoretical Sciences (ICTS), Bengaluru, India during a visit for participating in the program Frustrated Metals and Insulators (Code No. ICTS/frumi2022/9). Y.I. further acknowledges the use of the computing resources at HPCE, IIT Madras. H.O.J. thanks IIT Madras for a visiting faculty fellow position during which work on this project was carried out.

- 
- [1] D. A. Huse and A. D. Rutenberg, Classical antiferromagnets on the Kagomé lattice, *Phys. Rev. B* **45**, 7536 (1992).
- [2] D. J. J. Farnell, R. Darradi, R. Schmidt, and J. Richter, Spin-half Heisenberg antiferromagnet on two archimedean lattices: From the bounce lattice to the maple-leaf lattice and beyond, *Phys. Rev. B* **84**, 104406 (2011).
- [3] D. J. J. Farnell, O. Götze, J. Richter, R. F. Bishop, and P. H. Y. Li, Quantum  $s = \frac{1}{2}$  antiferromagnets on Archimedean lattices: The route from semiclassical magnetic order to nonmagnetic quantum states, *Phys. Rev. B* **89**, 184407 (2014).
- [4] Y.-Z. Zheng, Z. Zheng, and X.-M. Chen, A symbol approach for classification of molecule-based magnetic materials exemplified by coordination polymers of metal carboxylates, *Coord. Chem. Rev.* **258-259**, 1 (2014).
- [5] Y.-Z. Zheng, M.-L. Tong, W. Xue, W.-X. Zhang, X.-M. Chen, F. Grandjean, and G. J. Long, A “star” antiferromagnet: A polymeric iron(iii) acetate that exhibits both spin frustration and long-range magnetic ordering, *Angew. Chem. Int. Ed.* **46**, 6076 (2007).
- [6] H. Yamaguchi, D. Yoshizawa, T. Kida, M. Hagiwara, A. Matsuo, Y. Kono, T. Sakakibara, Y. Tamekuni, H. Miyagai, and Y. Hosokoshi, Magnetic-field-induced Quantum Phase in  $S = 1/2$  Frustrated Trellis Lattice, *J. Phys. Soc. Jpn.* **87**, 043701 (2018).
- [7] D. Betts, A new two-dimensional lattice of coordination number five, *Proc. N. S. Inst. Sci.* **40**, 95 (1995).
- [8] M. Norman, Copper tellurium oxides – a playground for magnetism, *J. Mag. Mag. Mater.* **452**, 507 (2018).
- [9] D. Inosov, Quantum magnetism in minerals, *Adv. Phys.* **67**, 149 (2018).
- [10] S. J. Mills, A. R. Kampf, A. G. Christy, R. M. Housley, G. R. Rossman, R. E. Reynolds, and J. Marty, Bluebellite and mojaveite, two new minerals from the central Mojave Desert, California, USA, *Mineralog. Mag.* **78**, 1325–1340 (2014).
- [11] A. R. Kampf, S. J. Mills, R. M. Housley, and J. Marty, Lead-tellurium oxysalts from Otto Mountain near Baker, California: VIII. fuettererite,  $\text{Pb}_3\text{Cu}_6^{2+}\text{Te}^{6+}\text{O}_6(\text{OH})_7\text{Cl}_5$ , a new mineral with double spangolite-type sheets, *Am. Mineralog.* **98**, 506 (2013).
- [12] F. Olmi, C. Sabelli, and R. Trosti-Ferroni, The crystal structure of sabelliite, *Eur. J. Mineral.* **7**, 1331 (1995).
- [13] S. L. Penfield, On spangolite, a new copper mineral, *Am. J. Sci.* **39**, 370 (1890).
- [14] H. A. Miers, Spangolite, a Remarkable Cornish Mineral, *Nature* **48**, 426 (1893).
- [15] C. Frondel, Crystallography of spangolite, *Am. Mineral.* **34**, 181 (1949).
- [16] F. C. Hawthorne, M. Kimata, and R. K. Eby, The crystal structure of spangolite, a complex copper sulfate sheet mineral, *Am. Mineral.* **78**, 649 (1993).
- [17] Y. Haraguchi, A. Matsuo, K. Kindo, and Z. Hiroi, Frustrated magnetism of the maple-leaf-lattice antiferromagnet  $\text{MgMn}_3\text{O}_7 \cdot 3\text{H}_2\text{O}$ , *Phys. Rev. B* **98**, 064412 (2018).
- [18] C. Venkatesh, B. Bandyopadhyay, A. Midya, K. Mahalingam, V. Ganesan, and P. Mandal, Magnetic properties of the one-dimensional  $S = \frac{3}{2}$  Heisenberg antiferromagnetic spin-chain compound  $\text{Na}_2\text{Mn}_3\text{O}_7$ , *Phys. Rev. B* **101**, 184429 (2020).
- [19] B. Saha, A. K. Bera, S. M. Yusuf, and A. Hoser, Two-dimensional short-range spin-spin correlations in the layered spin- $\frac{3}{2}$  maple leaf lattice antiferromagnet  $\text{Na}_2\text{Mn}_3\text{O}_7$  with crystal stacking disorder, *Phys. Rev. B* **107**, 064419 (2023).
- [20] T. Fennell, J. O. Piatek, R. A. Stephenson, G. J. Nilsen, and H. M. Rønnow, Spangolite: an  $s = 1/2$  maple leaf lattice antiferromagnet?, *J. Phys.: Condens. Matter* **23**, 164201 (2011).
- [21] Z. Y. Xie, J. Chen, J. F. Yu, X. Kong, B. Normand, and T. Xiang, Tensor renormalization of quantum many-body systems using projected entangled simplex states, *Phys. Rev. X* **4**, 011025 (2014).
- [22] P. Schmoll, C. Balz, B. Lake, J. Eisert, and A. Kshetri-mayum, Finite temperature tensor network algorithm for frustrated two-dimensional quantum materials (2022), [arXiv:2211.00121](https://arxiv.org/abs/2211.00121) [cond-mat.str-el].
- [23] P. Ghosh, T. Müller, and R. Thomale, Another exact ground state of a two-dimensional quantum antiferromagnet, *Phys. Rev. B* **105**, L180412 (2022).



- [24] P. Ghosh, T. Müller, Y. Iqbal, R. Thomale, and H. O. Jeschke, Effective spin-1 breathing kagome Hamiltonian induced by the exchange hierarchy in the maple leaf mineral bluebellite (2023), [arXiv:2301.05224](https://arxiv.org/abs/2301.05224) [cond-mat.str-el].
- [25] L. Gresista, C. Hickey, S. Trebst, and Y. Iqbal, Candidate quantum disordered intermediate phase in the Heisenberg antiferromagnet on the maple-leaf lattice, *Phys. Rev. B* **108**, L241116 (2023).
- [26] K. Iida, H. K. Yoshida, A. Nakao, H. O. Jeschke, Y. Iqbal, K. Nakajima, S. Ohira-Kawamura, K. Munakata, Y. Inamura, N. Murai, M. Ishikado, R. Kumai, T. Okada, M. Oda, K. Kakurai, and M. Matsuda,  $q = 0$  long-range magnetic order in centennialite  $\text{CaCu}_3(\text{OD})_6\text{Cl}_2 \cdot 0.6\text{D}_2\text{O}$ : A spin- $\frac{1}{2}$  perfect kagome antiferromagnet with  $J_1$ - $J_2$ - $J_d$ , *Phys. Rev. B* **101**, 220408 (2020).
- [27] H. Yamamoto, T. Sakakura, H. O. Jeschke, N. Kabeya, K. Hayashi, Y. Ishikawa, Y. Fujii, S. Kishimoto, H. Sagayama, K. Shigematsu, M. Azuma, A. Ochiai, Y. Noda, and H. Kimura, Quantum spin fluctuations and hydrogen bond network in the antiferromagnetic natural mineral henmilitite, *Phys. Rev. Mater.* **5**, 104405 (2021).
- [28] M. Fujihala, H. O. Jeschke, K. Morita, T. Kuwai, A. Koda, H. Okabe, A. Matsuo, K. Kindo, and S. Mitsuda, Birchite  $\text{Cd}_2\text{Cu}_2(\text{PO}_4)_2\text{SO}_4 \cdot 5\text{H}_2\text{O}$  as a model antiferromagnetic spin-1/2 Heisenberg  $J_1$ - $J_2$  chain, *Phys. Rev. Mater.* **6**, 114408 (2022).
- [29] Y. Iqbal, H. O. Jeschke, J. Reuther, R. Valentí, I. I. Mazin, M. Greiter, and R. Thomale, Paramagnetism in the kagome compounds  $(\text{Zn}, \text{Mg}, \text{Cd})\text{Cu}_3(\text{OH})_6\text{Cl}_2$ , *Phys. Rev. B* **92**, 220404 (2015).
- [30] D. W. Powell, R. G. Thomas, P. A. Williams, W. D. Birch, and I. R. Plimer, Choloalite: synthesis and revised chemical formula, *Mineralog. Mag.* **58**, 505 (1994).
- [31] S. Chillal, Y. Iqbal, H. O. Jeschke, J. A. Rodriguez-Rivera, R. Bewley, P. Manuel, D. Khalyavin, P. Steffens, R. Thomale, A. T. M. N. Islam, J. Reuther, and B. Lake, Evidence for a three-dimensional quantum spin liquid in  $\text{PbCuTe}_2\text{O}_6$ , *Nat. Commun.* **11**, 2348 (2020).
- [32] K. Koepnick and H. Eschrig, Full-potential nonorthogonal local-orbital minimum-basis band-structure scheme, *Phys. Rev. B* **59**, 1743 (1999).
- [33] J. P. Perdew, K. Burke, and M. Ernzerhof, Generalized gradient approximation made simple, *Phys. Rev. Lett.* **77**, 3865 (1996).
- [34] J. Eisert, M. Cramer, and M. B. Plenio, Colloquium: Area laws for the entanglement entropy, *Rev. Mod. Phys.* **82**, 277 (2010).
- [35] R. Orús, A practical introduction to tensor networks: Matrix product states and projected entangled pair states, *Ann. Phys. (NY)* **349**, 117 (2014).
- [36] P. Scholl, A. Kshetrimayum, J. Naumann, J. Eisert, and Y. Iqbal, Tensor network study of the spin- $\frac{1}{2}$  Heisenberg antiferromagnet on the shuriken lattice, *Phys. Rev. B* **107**, 064406 (2023).
- [37] T. Nishino and K. Okunishi, Corner Transfer Matrix Renormalization Group Method, *J. Phys. Soc. Jpn.* **65**, 891 (1996).
- [38] T. Nishino and K. Okunishi, Corner Transfer Matrix Algorithm for Classical Renormalization Group, *J. Phys. Soc. Jpn.* **66**, 3040 (1997).
- [39] R. Orús and G. Vidal, Simulation of two-dimensional quantum systems on an infinite lattice revisited: Corner transfer matrix for tensor contraction, *Phys. Rev. B* **80**, 094403 (2009).
- [40] J. Jordan, R. Orús, G. Vidal, F. Verstraete, and J. I. Cirac, Classical simulation of infinite-size quantum lattice systems in two spatial dimensions, *Phys. Rev. Lett.* **101**, 250602 (2008).
- [41] A. Kshetrimayum, M. Rizzi, J. Eisert, and R. Orús, Tensor network annealing algorithm for two-dimensional thermal states, *Phys. Rev. Lett.* **122**, 070502 (2019).
- [42] J. Naumann, E. L. Weerden, M. Rizzi, J. Eisert, and P. Scholl, An introduction to infinite projected entangled-pair state methods for variational ground state simulations using automatic differentiation (2024), [arXiv:2308.12358](https://arxiv.org/abs/2308.12358) [cond-mat.str-el].
- [43] P. Corboz, Variational optimization with infinite projected entangled-pair states, *Phys. Rev. B* **94**, 035133 (2016).
- [44] B. Ponsioen and P. Corboz, Excitations with projected entangled pair states using the corner transfer matrix method, *Phys. Rev. B* **101**, 195109 (2020).
- [45] B. Ponsioen, J. Hasik, and P. Corboz, Improved summations of  $n$ -point correlation functions of projected entangled-pair states, *Phys. Rev. B* **108**, 195111 (2023).
- [46] J. T. Haraldsen, T. Barnes, and J. L. Musfeldt, Neutron scattering and magnetic observables for  $S = 1/2$  spin clusters and molecular magnets, *Phys. Rev. B* **71**, 064403 (2005).
- [47] Y. Singh and D. C. Johnston, Singlet ground state in the spin- $\frac{1}{2}$  dimer compound  $\text{Sr}_3\text{Cr}_2\text{O}_8$ , *Phys. Rev. B* **76**, 012407 (2007).
- [48] D. L. Quintero-Castro, B. Lake, E. M. Wheeler, A. T. M. N. Islam, T. Guidi, K. C. Rule, Z. Izaola, M. Russina, K. Kiefer, and Y. Skourski, Magnetic excitations of the gapped quantum spin dimer antiferromagnet  $\text{Sr}_3\text{Cr}_2\text{O}_8$ , *Phys. Rev. B* **81**, 014415 (2010).
- [49] P. Ghosh, J. Seufert, T. Müller, F. Mila, and R. Thomale, Maple leaf antiferromagnet in a magnetic field, *Phys. Rev. B* **108**, L060406 (2023).
- [50] I. Affleck, Spin gap and symmetry breaking in  $\text{CuO}_2$  layers and other antiferromagnets, *Phys. Rev. B* **37**, 5186 (1988).
- [51] M. Oshikawa, M. Yamanaka, and I. Affleck, Magnetization Plateaus in Spin Chains: “Haldane Gap” for Half-Integer Spins, *Phys. Rev. Lett.* **78**, 1984 (1997).
- [52] J. Beck, J. Bodky, J. Motruk, T. Müller, R. Thomale, and P. Ghosh, Phase diagram of the  $J$ - $J_d$  Heisenberg Model on the Maple-Leaf Lattice: Neural networks and density matrix renormalization group (2024), [arXiv:2401.04995](https://arxiv.org/abs/2401.04995) [cond-mat.str-el].
- [53] M. Gembé, L. Gresista, H.-J. Schmidt, C. Hickey, Y. Iqbal, and S. Trebst, Noncoplanar orders and quantum disordered states in maple-leaf antiferromagnets (2024), [arXiv:2402.09400](https://arxiv.org/abs/2402.09400) [cond-mat.str-el].
- [54] P. Ghosh, Where is the spin liquid in maple-leaf quantum magnet? (2024), [arXiv:2401.09422](https://arxiv.org/abs/2401.09422) [cond-mat.str-el].
- [55] J. Sonnenschein, A. Maity, C. Liu, R. Thomale, F. Ferrari, and Y. Iqbal, Candidate quantum spin liquids on the maple-leaf lattice (2024), [arXiv:2404.05617](https://arxiv.org/abs/2404.05617) [cond-mat.str-el].
- [56] P. Scholl, S. S. Jahromi, M. Hörmann, M. Mühlhauser, K. P. Schmidt, and R. Orús, Fine grained tensor network methods, *Phys. Rev. Lett.* **124**, 200603 (2020).
- [57] P. C. G. Vlaar and P. Corboz, Efficient tensor network algorithm for layered systems, *Phys. Rev. Lett.* **130**, 130601 (2023).

- [58] L. Bennett, B. Melchers, and B. Proppe, *Curta: A general-purpose high-performance computer at ZEDAT, Freie Universität Berlin* (2020).
- [59] A. I. Liechtenstein, V. I. Anisimov, and J. Zaanen, Density-functional theory and strong interactions: Orbital ordering in Mott-Hubbard insulators, *Phys. Rev. B* **52**, R5467 (1995).

## Appendix A: Density functional theory based energy mapping

We use all electron density functional theory calculations with a full potential local orbital (FPLO) basis set [32]. For the prediction of the hydrogen atom positions, we use a generalized gradient approximation (GGA) exchange correlation functional [33]. We determine the Heisenberg Hamiltonian parameters from total energies where we correct for the strong electronic correlations on the  $\text{Cu}^{2+}$   $3d$  orbitals by a DFT+U functional [59]. For the energy mapping approach, we classify all 4096 possible spin configurations for the twelve  $\text{Cu}^{2+}$  ions in the unit cell after removing the symmetry. We find that the 364 distinct classical energies allow us to resolve twelve Heisenberg Hamiltonian parameters. We fix the Hund's rule coupling for Cu  $3d$  as  $J_H = 1$  eV, in agreement with many previous studies [26, 31]. We then perform the energy mapping approach for five values of the onsite interaction value  $U$  (see Fig. 1c). We choose the appropriate value for spangolite by demanding that the Curie-Weiss temperature calculated as

$$\theta_{\text{CW}} = \frac{1}{3}S(S+1)(J_1 + J_2 + J_3 + J_4 + J_5 + J_{15} + J_{16} + J_{17} + J_{18} + J_{19} + J_{21} + J_{23}) \quad (\text{A1})$$

agree with the experimental value of  $\theta_{\text{CW}} = -38$  K [20]. The resulting  $U = 7.52$  eV is rather typical.

## Appendix B: Maple-leaf lattice definition

Assuming a Cartesian coordinate system that sets the reference, the lattice vectors are given by

$$\vec{a}_1 = -\frac{\sqrt{7}}{2} \begin{pmatrix} 1 \\ \sqrt{3} \end{pmatrix} \quad \vec{a}_2 = \sqrt{7} \begin{pmatrix} 1 \\ 0 \end{pmatrix}. \quad (\text{B1})$$

Here, the lattice constant is set to  $a = 1$ . Furthermore, the six-site basis of the maple-leaf lattice is defined in Fig. 6. A fully translational system therefore consists of a single unit cell with six spins. The basis is spanned by

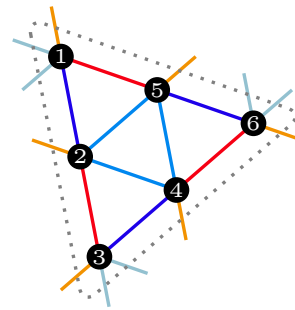


FIG. 6. Definition of one unit cell, the six-site basis of the maple-leaf lattice.

the six basis vectors

$$\begin{aligned} \vec{b}_1 &= \begin{pmatrix} 0 \\ 0 \end{pmatrix} & \vec{b}_4 &= \frac{1}{\sqrt{7}} \begin{pmatrix} 3 \\ -2\sqrt{3} \end{pmatrix} \\ \vec{b}_2 &= \frac{1}{2\sqrt{7}} \begin{pmatrix} 1 \\ -3\sqrt{3} \end{pmatrix} & \vec{b}_5 &= \frac{1}{2\sqrt{7}} \begin{pmatrix} 5 \\ -\sqrt{3} \end{pmatrix} \\ \vec{b}_3 &= \frac{1}{\sqrt{7}} \begin{pmatrix} 1 \\ -3\sqrt{3} \end{pmatrix} & \vec{b}_6 &= \frac{1}{\sqrt{7}} \begin{pmatrix} 5 \\ -\sqrt{3} \end{pmatrix}. \end{aligned} \quad (\text{B2})$$

## Appendix C: Tensor network details

### 1. Ground state calculations

In order to represent the wave function of the ground state, we employ the iPES ansatz. The tensor coefficients, that ultimately represent the target wave function in the thermodynamic limit are determined by a simple update procedure. It is based on evolving an initial wave function under imaginary time evolution to project out the ground state [21, 40]. Due to the chosen coarse-graining of  $J_1$  bonds, a single update steps includes six lattice sites in triangle configurations at a time. This is visualized in Fig. 2b. In order to keep the bond dimension constant, the network has to be truncated back to  $\chi_B$  after each application of the imaginary time evolution gate  $e^{-\delta\tau H}$ . Although the simple update is an approximate scheme and treats the environment of a cluster only in mean-field approximation, it is expected and has proven to work reliably for frustrated quantum lattice systems in two dimensions.

### 2. Thermal state calculations

In contrast to ground state simulations, the local spin degrees of freedom have to be doubled, such that the system is described by a thermal density matrix. The iPES ansatz for state vectors has been recently extended to the realm of operators, enabling the efficient simulation of thermal states of frustrated systems using iPESO [22]. Here, the algorithm used to obtain a thermal density matrix  $\rho(\beta)$  at inverse temperature  $\beta$  is again based on

the simple update and Trotterization of the Hamiltonian. Starting from an infinite-temperature state  $\rho(\beta = 0)$ , where the thermal density matrix is simply a tensor product of local identity matrices, the system is cooled down to the desired final temperature  $\beta$ . This procedure is implemented by successive cooling steps with infinitesimal temperature  $\delta\beta$  to keep the overall errors controllable. This can be done in a similar fashion as in the simple update ground state optimization and it is visualized in Fig. 2 c. Again, after the evolution with the gate  $e^{-\delta\beta H}$ , the resulting iPESO network is truncated to the bulk bond dimension  $\chi_B$ . The accumulated truncation error  $\varepsilon$  of the full procedure can be used to probe the accuracy of the simulations [22].

### 3. Calculation of expectation values

In order to compute expectation values, the honeycomb structure of the iPES/iPESO ansatz can be mapped to a regular square lattice with lattice vectors as shown in Fig. 1 a. The resulting tensor network on the square lattice is known as an *infinite projected entangled pair*

*state* (iPEPS) or *infinite projected entangled pair operator* (iPEPO) respectively, which includes six spins of the original MLL on every lattice site. This additional step is required to compute effective fixed-point environments of the infinite MLL, e.g. by a regular *corner transfer matrix renormalization group* (CTMRG) procedure, as shown in Fig. 2 d. Expectation values on the MLL can then be accurately computed by the evaluation of single-site and three-site expectation values on the coarse-grained square lattice, corresponding to the two different types of simplex configurations in the iPES/iPESO ansatz. The approximations in the contraction of the infinite 2D lattice are controlled by a bond dimension for the effective environment tensors, denoted by  $\chi_E$ . In practise, this parameter has to be large enough so that expectation values are well converged. Besides taking the full CTMRG environment into account for the calculation of expectation values, it is also possible to only use a mean-field (MF) environment. This environment is readily available from the simple update for both ground and thermal states. MF expectation values are computationally much cheaper and have to be used for large bond dimensions due to the high computational cost of the CTMRG routine.